

Accurate Model of the Projected Velocity Distribution of Galaxies in Dark Matter Halos

Han Aung¹, Daisuke Nagai¹, Eduardo Rozo², Brandon Wolfe², Susmita Adhikari^{3,4}

¹*Department of Physics, Yale University, New Haven, CT 06520, USA*

²*Department of Physics, University of Arizona, Tucson, AZ 85721 USA*

³*Indian Institute of Science Education and Research, Pune, Maharashtra, 411008, India*

⁴*Department of Astronomy and Astrophysics, University of Chicago, Chicago, IL 60637, USA*

27 January 2023

ABSTRACT

We present a percent-level accurate model of the line-of-sight velocity distribution of galaxies around dark matter halos as a function of projected radius and halo mass. The model is developed and tested using synthetic galaxy catalogs generated with the UniverseMachine run on the Multi-Dark Planck 2 N-body simulations. The model decomposes the galaxies around a cluster into three kinematically distinct classes: orbiting, infalling, and interloping galaxies. We demonstrate that: 1) we can statistically distinguish between these three types of galaxies using only projected line-of-sight velocity information; 2) the halo edge radius inferred from the line-of-sight velocity dispersion is an excellent proxy for the three-dimensional halo edge radius; 3) we can accurately recover the full velocity dispersion profile for each of the three populations of galaxies. Importantly, the velocity dispersion profiles of the orbiting and infalling galaxies contain five independent parameters — three distinct radial scales and two velocity dispersion amplitudes — each of which is correlated with mass. Thus, the velocity dispersion profile of galaxy clusters has inherent redundancies that allow us to perform nontrivial systematics checks from a single data set. We discuss several potential applications of our new model for detecting the edge radius and constraining cosmology and astrophysics using upcoming spectroscopic surveys.

1 INTRODUCTION

The abundance of galaxy clusters as a function of mass makes them powerful cosmological probes. One way to infer cluster masses is using galaxy dynamics (Evrard et al. 2008; Bocquet et al. 2015). However, the utility of cluster samples can be limited by systematic uncertainties associated with nonlinear cluster astrophysics (Allen et al. 2011; Pratt et al. 2019). One of the new frontiers in cluster cosmology exploits the outskirts of galaxy clusters, where the impacts of poorly understood baryonic effects are modest (Walker et al. 2019). Recent studies show that the phase space information around and outside the galaxy clusters enables dynamical mass estimation from larger regions around the cluster (Hamabata et al. 2019), can place constraints on modified gravity (Lam et al. 2012; Zu et al. 2014), and enable the use of halo boundaries as a standard ruler (Wagoner et al. 2021).

Recent work demonstrated that the phase space structure of the halo exhibits two different populations of galaxies: 1) orbiting galaxies that have been inside the cluster; and 2) infalling galaxies which have never been inside the cluster (Aung et al. 2021). Moreover, there is a bonafide edge radius beyond which no orbiting galaxies can be found (Bakels et al. 2021). This edge radius provides a better definition of halo radius than traditional overdensity definitions: it denotes the halo boundary within which all orbiting dark matter particles and subhalos reside. The halo edge radius is intimately related to the traditional splashback radius. While the splashback radius was originally defined in terms of the steepest slope of the halo’s density profile (Diemer & Kravtsov 2014; Adhikari et al. 2014; More et al. 2015), modern definitions rely on a spe-

cific percentile of the distribution of orbiting particle apocenters, typically in the range 75% to 87% so as to match the “steepest slope” definition (Diemer et al. 2017). The halo edge radius is the smallest possible 100-percentile splashback radius.

The edge radius of galaxy clusters has been detected using the Sloan Digital Sky Survey redMaPPer cluster catalog (Tomooka et al. 2020). Specifically, the edge radius is seen as a “break” in the velocity dispersion profile of galaxy clusters. Because the amplitude of the velocity dispersion profile must be correlated with the halo edge radius (more massive halos are bigger), one can use the halo edge radius as a standard ruler (Wagoner et al. 2021). A measurement of the amplitude of the velocity dispersion profile allows us to infer the halo edge radius in Mpc, while measurements of the profile as a function of angle allow us to determine the angle spanned by the halo edge radius. Together, these two pieces of data allow us to measure the distance to galaxy clusters. Forecasts show that the next generation of spectroscopic surveys such as Dark Energy Spectroscopic Instrument (DESI, DESI Collaboration et al. 2016) will provide enough statistics to measure the Hubble constant with percent level precision using this technique (Wagoner et al. 2021).

Actually achieving a percent level measurement of the Hubble constant requires controlling the theoretical and observational systematics impacting the measurement with sub-percent level precision (Wagoner et al. 2021). Current major sources of uncertainties in measuring line-of-sight velocity dispersion profile are: 1) accurate modeling of the nonlinear dynamics of dark matter particles in the infall and virialized regions (Lam et al. 2013; Zu &

arXiv:2204.13131v2 [astro-ph.CO] 26 Jan 2023

Weinberg 2013); 2) recovery of 3D phase space of galaxies from 2D measurements in the presence of projection effects (Farahi et al. 2016); and 3) velocity bias which primarily impacts galaxies in clusters due to dynamical friction and baryonic effects (Lau et al. 2010; Munari et al. 2013; Wu et al. 2013; Anbajagane et al. 2022). In this paper, we provide an accurate model of the projected phase space structure of line-of-sight velocities. Further, we demonstrate that our model allows deriving unbiased estimates of critical halo properties for our clusters, including the halo edge radius, as well as the spatial and dynamical profiles of orbiting and infalling galaxies.

In detail, we use synthetic galaxy catalogs generated using the UniverseMachine (Behroozi et al. 2019) run on the Multi-Dark Planck 2 N-body simulation (Klypin et al. 2016) to motivate parametric models for the surface number density and line-of-sight velocity dispersions of three kinematically distinct populations of galaxies in and around halos: orbiting, infalling, and background. As we demonstrate below, our model enables us to: 1) use the distinct dynamical signatures of orbiting, infalling, and background galaxies to statistically separate these three populations across all cluster radii using line-of-sight velocity data; 2) robustly infer the three-dimensional halo edge radius from line-of-sight velocity dispersion measurements; and 3) use the radial and velocity scales associated with the orbiting and infalling galaxy populations, to enable accurate detection of the edge radius. We note the possibility of using infalling galaxies for these purposes is particularly interesting, as infalling galaxies have spent little time in the halo environment, and are therefore more likely to be free from velocity bias due to the baryonic physics in the halo environment.

Our paper is laid out as follows. We describe the simulation and mock galaxy catalog in §2. We explain the classification of orbiting and infalling galaxies and how they impact the velocity dispersion and cluster mass measurements in §3. We present our new model of the projected phase space structure of dark matter halos in §4, and verify the validity of this model using the mock galaxy catalog in §5. We will then discuss applications of our model in §6. Our main findings are summarized in §7.

2 METHODOLOGY

2.1 Mock Catalogs

We analyze mock galaxy catalogs constructed using the *MDPL2* (Multi-Dark Planck) DM-only *N*-body simulation. The simulation was performed with the L-GADGET-2 code, a version of the publicly available cosmological code GADGET-2 (Springel 2005). The simulation has a box size of 1 Gpc/h, with a physical force resolution that decreases from 13 kpc/h at high-*z* to 5 kpc/h at low-*z*. The particle mass is $1.51 \times 10^9 M_\odot/h$ with 3840^3 particles in the box. It assumes the *Planck* 2013 cosmology with $\Omega_m = 0.307$, $\Omega_\Lambda = 0.693$, $\sigma_8 = 0.823$, and $H_0 = 68 \text{ km(s Mpc)}^{-1}$. The halos and subhalos are identified using the Rockstar 6D phase space halo finder (Behroozi et al. 2013a), and the merger tree is built using the Consistent-Tree algorithm (Behroozi et al. 2013b). More details of the simulation can be found in Klypin et al. (2016).

The mock galaxy catalog is constructed using the UniverseMachine (Behroozi et al. 2019), which pastes galaxies into halos and subhalos. In this algorithm, the in-situ star formation rate is parameterized as a function

of halo mass, halo assembly history, and redshift. Model galaxies are grafted directly onto halos and subhalos in the Rockstar merger trees from MDPL2 simulation. The stellar mass of the halo is then computed by integrating the star formation rates over the time steps of the simulation output, tracking the merger history of the halo. The algorithm forces the statistical properties of the resulting galaxy distribution to match the following observational data across cosmic times: (i) stellar mass functions; (ii) cosmic star-formation rates and specific star-formation rates; (iii) quenched fractions; (iv) correlation functions for all, quenched, and star-forming galaxies; and (v) measurements of the environmental dependence of central galaxy quenching, using isolation criteria to identify centrals and a counts-in-cylinders-based quantification of ~ 5 Mpc density. These measurements are matched across a broad range of redshifts ($0 < z < 10$).

For this study, we restrict ourselves to dark matter halos with $M_{200m} > 10^{14} M_\odot/h$, focusing on the high mass clusters. We also restrict ourselves to galaxies with a stellar mass $M_* > 10^9 M_\odot/h$. Orphan galaxies are necessary to correct for artificially disrupted subhalos in the simulations and are added by extrapolating the position and velocity of disrupted subhalos according to Jiang & van den Bosch (2014). Because we expect the systematic uncertainty in the model to increase near halo centers, where the fraction of orphan galaxies is high, we will ignore the cluster core when testing our model.

2.2 Measurement

Using the distant observer approximation, we select the *z* axis of the simulation box as the line-of-sight. Each halo has a central galaxy that shares the halo's position and velocity. The projected radial distance between the cluster's central galaxy and any other galaxy is $R = \sqrt{(x - x_{\text{cen}})^2 + (y - y_{\text{cen}})^2}$, and the 3D radial distance is $r = \sqrt{(x - x_{\text{cen}})^2 + (y - y_{\text{cen}})^2 + (z - z_{\text{cen}})^2}$. We will consistently use the variable *R* for projected distances, and the variable *r* for three-dimensional distances. The relative line-of-sight velocity (LOS) of a simulated galaxy is

$$v_{\text{LOS}} = (v_z - v_{z,\text{cen}}) + aH(z)d_{\text{com,LOS}}, \quad (1)$$

where $v_z - v_{z,\text{cen}}$ is the peculiar velocity of the galaxy with respect to the cluster, and the second term describes the velocity due to the expansion of the universe where $d_{\text{com,LOS}}$ is the comoving distance between the cluster and the galaxy along the LOS. We apply a maximum velocity cut $|v_{\text{LOS}}| < 3000 \text{ km s}^{-1}$ for the galaxies used to study the velocity distribution.¹ Error estimates for all quantities we measure in the simulation are obtained using the jackknife method. Specifically, we split the simulation box into 100 different regions using the comoving *z*-coordinate. That is, halos with $z_{\text{cen}} = [10(i-1), 10i]\text{Mpc}/h$ in comoving units belongs to the *i*-th subsample. All the subsamples are then aggregated together to measure the mean profiles and jackknife errors.

¹ This velocity cut is equivalent to 3-5 times the velocity dispersion of the clusters involved in the studies, large enough to encompass all galaxies associated with clusters.

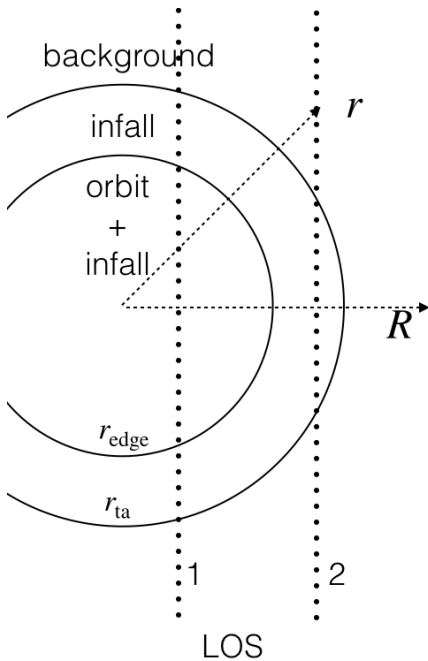


Figure 1. A schematic diagram showing the split of the galaxy density field near a halo into its three components: orbiting galaxies, infalling galaxies, and background galaxies. The line of sight velocity dispersion profile for lines of sight near the halo center (e.g., LOS 1) receives contributions from all three types of galaxies, whereas more distant lines of sight (e.g., LOS 2) contain only infall and background galaxies. The transition between these two limits occurs at the halo’s edge radius.

3 CLASSIFICATION OF ORBITING AND INFALLING GALAXIES

We classify the galaxies in the vicinity of a massive dark matter halo into 3 different categories: *orbiting*, *infalling* and *background* as follows. We define the turnaround radius r_{ta} to be the radius where the average physical radial velocity is zero ($\langle v_r \rangle = 0$). Galaxies at radial separations $r \geq r_{\text{ta}}$ are defined to be background galaxies. Galaxies with radial separations $r < r_{\text{ta}}$ that have never experienced pericentric passages ($v_r < 0$) inside the central halo are defined as infalling, while galaxies that have experienced pericentric passages are defined as orbiting. In 3D, the background galaxies are clearly separated from the orbiting and infalling components. Between the halo edge radius — defined as the maximal radial separation of the orbiting galaxies — and the turnaround radius, one finds only infalling galaxies by definition. Inside the edge radius, orbiting and infalling galaxies mix. A sketch of this setup is shown in Fig. 1.

Figure 2 shows the orbiting (blue) and infalling (red) galaxy populations in the v_r – r plane, where v_r is the physical radial velocity without the Hubble flow. Background galaxies are not shown because r_{ta} is larger than the radial range of the figure. We see infalling galaxies have an ever-increasing inwards peculiar velocity while orbiting galaxies disperse around the zero radial velocity line. The radial velocity dispersion of the orbiting galaxies decreases with increasing radius. We note that the infall stream protrudes deeply into the halo, well past the edge radius of the halo, and that the orbiting and infalling populations are mixed in phase space at small radii.

We define the combination of orbiting and infalling populations around a halo as “dynamically associated galax-

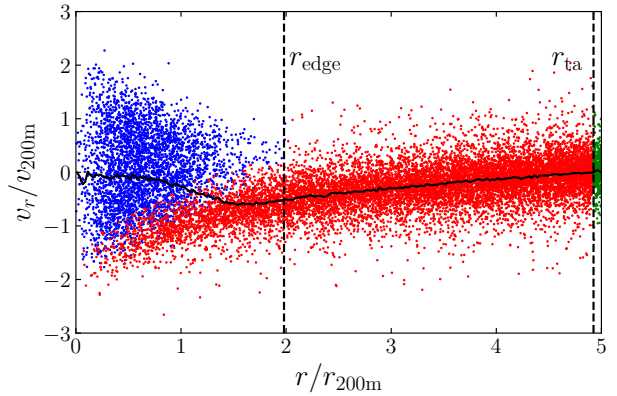


Figure 2. Peculiar radial velocity of galaxies as a function of radius. Orbiting galaxies are denoted as blue, infalling galaxies as red, and background galaxies as green. The halo edge radius is defined as the smallest radius containing all orbiting galaxies. Infalling galaxies start at the turnaround radius and continue all the way to the inner radii, with more negative radial velocities relative to the orbiting population. Galaxies lie outside of the turnaround radius where the average radial velocity (black line) is larger than zero.

ies” (indicated as “da”), as their dynamics are significantly impacted by the gravity of the halo. Fig. 3 shows the line-of-sight velocity dispersion profile of dynamically associated galaxies in simulation (left panel) and observation (right panel), as measured in Tomooka et al. (2020). The two profiles share similar features: the dispersion profile first decreases with increasing radius, eventually flattening out past the presumed edge radius of the halo/cluster. One of the key goals of this work is to demonstrate that this feature can indeed be identified with the halo edge radius, as advocated in Tomooka et al. (2020).

4 A MODEL OF PROJECTED DARK MATTER PHASE SPACE STRUCTURES

Given that we cannot classify which galaxies are orbiting, infalling or interlopers in the observed galaxy catalog, we improve upon the heuristic model of Tomooka et al. (2020) by characterizing the density and velocity dispersion profile of each type of galaxy in numerical simulations. Specifically, we provide parameterizations that accurately describe the distribution of galaxy line-of-sight velocities as a function of projected radius, averaged over halos of fixed mass. We will leave halo-to-halo variations in these velocity profiles as a subject for future studies. Our model takes the form

$$P(v, R) = f_{\text{orb}}(R)G(v, \sigma_{\text{orb}}(R)) + f_{\text{inf}}(R)E(v, \sigma_{\text{inf}}(R)) + (1 - f_{\text{orb}}(R) - f_{\text{inf}}(R))G(v, \sigma_{\text{bg}}), \quad (2)$$

where $G(v, \sigma)$ — used to describe both orbiting and background galaxies — is a Gaussian distribution of mean zero and variance of σ^2 . The infall population is modeled using the sech function,

$$E(v, \sigma) = \frac{1}{2\sigma} \operatorname{sech}\left(\frac{\pi v}{2\sigma}\right), \quad (3)$$

which has zero mean and variance of σ^2 . We will compare these distributions against the simulation data in §5.

To model the velocity distribution $P(v)$ using equation 2 we must also specify the width parameters σ_{orb} , σ_{inf} , and

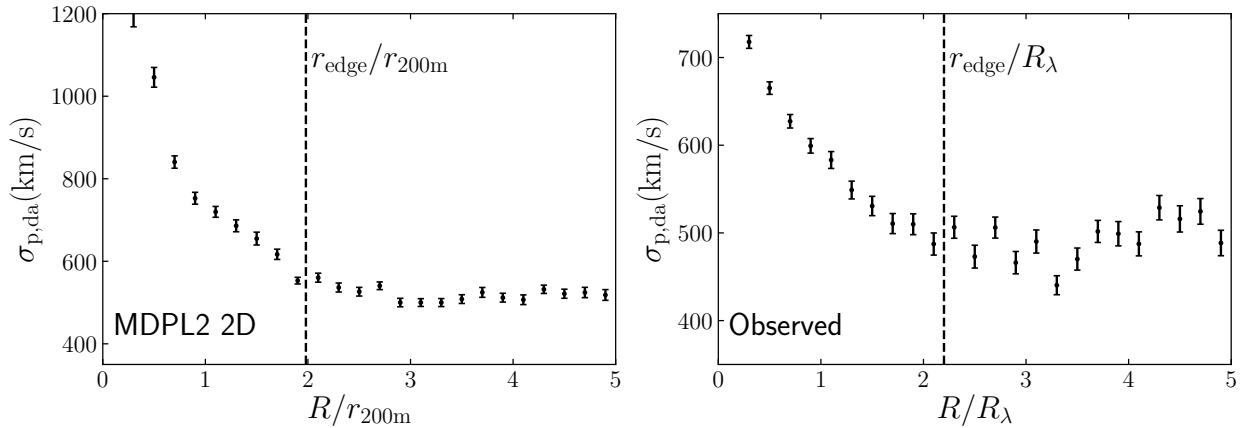


Figure 3. *Left panel:* Profile of the LOS velocity dispersion of dynamically associated galaxies (orbiting+infalling) as a function of projected radius in the mock catalog. The velocity dispersion monotonically decreases until R_{edge} , after which the profile flattens. *Right panel:* Fig 2 of Tomooka et al. (2020), showing the “kink” in the observed dispersion profile similar to the feature shown in the left panel, where R_{λ} is the radius inside which velocity dispersion profile is increasing and outside which it is constant.

σ_{bg} which must depend on radius. We parameterize the radial profiles of the velocity dispersions as:

$$\sigma_{\text{orb}}(R) = \sigma_{0,\text{orb}} \left(q_{\text{orb}} e^{-R/R_{\text{orb}}} + 1 \right), \quad (4)$$

$$\sigma_{\text{inf}}(R) = \sigma_{0,\text{inf}} \left(q_{\text{inf}} e^{-R/R_{\text{inf}}} + 1 \right), \quad (5)$$

$$\sigma_{\text{bg}}(R) = \sigma_{\text{bg}}, \quad (6)$$

where the amplitudes of the velocity dispersion profiles scale with mass as:

$$\sigma_{0,\text{inf}} = \sigma_{\text{p,inf}} \left(\frac{M}{M_{\text{p}}} \right)^{\alpha_{\text{inf}}}, \quad (7)$$

$$\sigma_{0,\text{orb}} = \sigma_{\text{p,orb}} \left(\frac{\sigma_{0,\text{inf}}}{\sigma_{\text{p,inf}}} \right)^{\alpha_{\text{orb}}}, \quad (8)$$

$$\sigma_{\text{bg}} = \sigma_{\text{p,bg}} \left(\frac{\sigma_{0,\text{inf}}}{\sigma_{\text{p,inf}}} \right)^{\alpha_{\text{bg}}}, \quad (9)$$

where M_{p} is a pivot mass, chosen to be $1.24 \times 10^{14} M_{\odot}/h$, the median mass of the halos we selected. σ_{p} 's and α 's are scaling parameters associated with the velocity dispersion of the orbiting and infalling populations. Note that in the above expressions we chose to scale the orbiting and background velocity dispersion with $\sigma_{\text{p,inf}}$ rather than the halo mass. q_{orb} and q_{inf} denote the ratio of velocity dispersion at the center of the cluster to the outskirts. We adopt these functions based on the features in the velocity dispersion profiles measured from the simulated data as explained below.

This choice is motivated by the fact that the different scaling relations are driven by gravity and are therefore relatively robust to selection effects. If this is the case, then one can simply tie σ_{inf} to a cluster observable (mass, richness, SZ decrement, etc), while preserving the velocity dispersion scalings. In other words, it is our hope that with this parameterization, the primary impact of cluster selection effects will be largely (though possibly not entirely) limited to the impact of the cluster scaling relation between σ_{inf} and the cluster observable. As to why we chose σ_{inf} as our base variable, as opposed to, say, σ_{orb} , we anticipate that the relation between $\sigma_{\text{p,inf}}$ and halo mass will be very robust to baryonic physics. Of course, the relation between, say, the orbiting and infalling velocity dispersions could easily be impacted by baryonic physics, but this effect is now contained within a scaling relation that is directly observable.

The radial dependencies in the above equations are chosen based on the qualitative features of the profiles in simulations. In particular, we found that σ_{orb} and σ_{inf} both decrease with increasing radius with a characteristic length scale R_{orb} and R_{inf} . Both profiles asymptote to a constant, and the relative amplitude of the constant “shelf” to the peak at small radii is characterized by the parameters q_{orb} and q_{inf} . The amplitude of all three velocity dispersion profiles scale with mass either because (a) the galaxies are virialized, (b) the infall velocity is sensitive to the halo mass, or (c) the clustering bias at large scales is dependent on mass.

Finally, all the radial scales of the infalling and background galaxies scale with mass and/or velocity dispersion. We again use the infall velocity dispersion as our base variable, so that:

$$R_{\text{edge}} = R_{\text{p,edge}} \left(\frac{\sigma_{0,\text{inf}}}{\sigma_{\text{p,inf}}} \right)^{\alpha_{\text{edge}}}, \quad (10)$$

$$R_{\text{orb}} = R_{\text{p,orb}} \left(\frac{\sigma_{0,\text{inf}}}{\sigma_{\text{p,inf}}} \right)^{\alpha_{\text{orb}}}, \quad (11)$$

$$R_{\text{inf}} = R_{\text{p,inf}} \left(\frac{\sigma_{0,\text{inf}}}{\sigma_{\text{p,inf}}} \right)^{\alpha_{\text{rinf}}}, \quad (12)$$

where R_{p} 's and α 's are fitted parameters associated with the shape of velocity dispersion of the orbiting and infalling populations. The scaling relations in Eq. (10)–Eq. (12) allow us to stack halos with different masses and provide a method to convert the velocity dispersions into physical scales.

The fraction of each type of galaxy is given by the ratio of the surface number densities (Σ):

$$f_x = \frac{\Sigma_x}{\Sigma_{\text{orb}} + \Sigma_{\text{inf}} + \Sigma_{\text{bg}}}, \quad (13)$$

where f_x is the fraction of galaxies of type “x”, which can be orbiting (orb), infalling (inf), or background (bg). Note that the fraction f_x is invariant under a multiplicative constant being applied to all surface density profiles. We use this invariance to arbitrarily normalize the orbiting profile so that $\rho_{\text{orb}} = 1$ at $r = 0$. Consequently, the normalization parameters describing the infalling and background surface density profiles characterize only the normalization relative to Σ_{orb} .

The *dimensionless* projected surface density of orbiting

galaxies is given by:

$$\Sigma_{\text{orb}}(R) = \int_0^{l_{\text{edge}}} \rho_{3\text{d}}(r) \frac{dl}{R_{\text{edge}}}, \quad (14)$$

where $l = \sqrt{r^2 - R^2}$ and $l_{\text{edge}} = \sqrt{\max\{R_{\text{edge}}^2 - R^2, 0\}}$. The dimensionless 3D density profile of orbiting galaxies is modeled following Diemer & Kravtsov (2014):

$$\rho_{3\text{d}}(r) = \exp\left(-\frac{2}{\alpha} \left[\left(\frac{r}{r_s}\right)^\alpha - 1\right]\right) \left[1 + \left(\frac{r}{r_t}\right)^\beta\right]^{-\gamma/\beta}, \quad (15)$$

where $\beta = 4$ and $\gamma = 6$ control the steepening of the slope near the splashback radius, and $\alpha = 0.155 + 0.0095\nu^2$ determines how quickly the inner profile slope steepens. These parameter estimations are directly taken from the dark matter density profile fits from Diemer & Kravtsov (2014). The peak-height ν is defined as $\delta_c/\sigma(M, z)$, where δ_c is the critical overdensity collapse threshold, and $\sigma(M, z)$ is the variance of the linear density field on the scale of the halo. r_s is the scale radius where the concentration of the halo $r_{200\text{m}}/r_s$ is given as a function of mass following Duffy et al. (2008). $r_t = R_{\text{edge}}/k_t$, and k_t denotes the ratio of edge radius to the splashback radius as defined by steepest density slope. We parameterize Σ_{inf} and Σ_{bg} as

$$\Sigma_{\text{inf}} = s_1 (R/R_{\text{edge}})^{s_2}, \quad (16)$$

$$\Sigma_{\text{bg}} = s_3 (R/R_{\text{edge}})^{s_4}, \quad (17)$$

where s_1 and s_3 provide the normalization of the infalling and background projected profiles relative to the orbiting contribution, and s_2 and s_4 provide the logarithmic slope respective to the projected radius. The normalization for the projected profiles depends on the mass of the halo. We, thus, parametrize them as

$$s_1 = s_{1\text{p}} \left(\frac{\sigma_{0,\text{inf}}}{\sigma_{\text{p,inf}}}\right)^{\alpha_{s1}}, \quad (18)$$

$$s_3 = s_{3\text{p}} \left(\frac{\sigma_{0,\text{inf}}}{\sigma_{\text{p,inf}}}\right)^{\alpha_{s3}}. \quad (19)$$

We found that s_2 and s_4 do not have a strong mass dependence, and including them as additional parameters adds unnecessary degeneracy. Thus, we decide to ignore mass dependence.

In addition, we define Σ_{da} as the surface number density of dynamically associated galaxies (infall+orbiting), and Σ_{all} as the surface number density of all (orbiting+infalling+background) galaxies. We emphasize we are not interested in highly accurate descriptions of the density profiles themselves. Rather, we wish to achieve parametric descriptions that are “good enough” to accurately infer the fraction of orbiting/infalling galaxies as a function of radius, as this is the quantity that goes into our model. We perform this comparison in §5.

The summary of our model is described in Fig. 4, and the free parameters associated with each of the quantities are listed in Table 1.

5 MODEL VALIDATION

We now demonstrate that the model from §4 allows us to recover the 3-dimensional structure of orbiting, infalling, and background galaxies from the line-of-sight-projected observables in simulations.

Key quantity	Parameters	Equations
Σ	$k_t, s_{1\text{p}}, s_2, s_{3\text{p}}, s_4$	Eqs. (14) to (17)
σ_{inf}	$\alpha_{\text{inf}}, \sigma_{\text{p,inf}}, q_{\text{inf}}$	Eq. (5)
σ_{orb}	$\alpha_{\text{orb}}, \sigma_{\text{p,orb}}, q_{\text{orb}}$	Eq. (4)
σ_{bg}	α_{bg}	Eq. (6)
R_{edge}	$R_{\text{p,edge}}, \alpha_{\text{edge}}$	Eq. (10)
R_{orb}	$R_{\text{p,orb}}, \alpha_{\text{rorb}}$	Eq. (11)
R_{inf}	$R_{\text{p,inf}}, \alpha_{\text{rinf}}$	Eq. (12)

Table 1. The table lists the key physical quantities (surface densities Σ , velocity dispersions σ , and distance scales R), the free parameters associated with the quantities along with the equations that describe their relations. To see how the key quantities construct the final distribution function, see the summary in Fig. 4. For the results in §5, all parameters are fitted.

The likelihood of the projected galaxy velocity data is

$$\mathcal{L} = \prod_i P(v_i | R_i, M_i), \quad (20)$$

where $P(v_i | R_i)$ is the probability distribution in equation 2. The product is over all galaxies within a given projected radius of the cluster and within a velocity cut $v \leq 3,000$ km/s. The variable v_i is the line-of-sight velocity of galaxy i , R_i is the projected radius of galaxy i , and M_i is the mass of the central halo of galaxy i . Note all these quantities are observables, with the exception of the halo mass. For our analysis, we will use $M_{200\text{m}}$ (and $r_{200\text{m}}$) as known quantities from the halo catalog. But, when analyzing real data, the halo mass would be replaced by an observable halo-mass proxy (e.g., richness, integrated SZ signal, or X-ray luminosity). In other words, for the purposes of our analysis, we are treating halo mass only as a mass proxy: our analysis does not rely on the fact that our “mass proxy” is the bonafide halo mass. We will characterize the impact of selection effects and the use of observable mass proxies on our results in future work. For now, we restrict ourselves to demonstrating that in the absence of such complications, our modeling framework accurately describes the velocity profile of halos.

When analyzing data, we ignore all galaxies in the cluster’s central region ($R \lesssim 0.3r_{200\text{m}}$). The fraction of orphan galaxies in the simulation increases towards the halo center, rising from $\approx 15\%$ at $R = 0.3r_{200\text{m}}$ to 40% at $R < 0.05r_{200\text{m}}$ as shown in Fig. 5. By restricting our analysis to radii $R \geq 0.3r_{200}$, we drastically reduce the impact of orphan galaxies on the galaxy velocity dispersion and distribution profiles which vary by no more than 3% with or without orphans. We note that baryonic physics can also change the velocity dispersion of the galaxies within the 3D radius $r \lesssim 0.2r_{200\text{m}}$ (Lau et al. 2010), so our $R \geq 0.3r_{200\text{m}}$ cut should also help in this regard.

We use the MCMC sampler Emcee (Foreman-Mackey et al. 2013) to create a realization of the posterior of our model parameters given a simulated dataset. We adopt the maximum likelihood point as our best-fit model. During the fit, we applied a prior such that all radii and the surface number densities were positive. Furthermore, we demand $\sigma_{\text{p,bg}} > \sigma_{\text{p,orb}(0)} + 500$ km/s to distinguish between the Gaussian of the background from that of the orbiting galaxies in the fit. We checked that our results are robust when changing 500 to [300 – 1000]km/s.

Fig. 6 compares the velocity distribution $P(v|R)$ obtained for orbiting and infalling galaxies using our likelihood model (dashed curves) to that inferred from splitting galaxies into orbiting, infalling, and background galaxies using 3D information and particle orbits as described in §

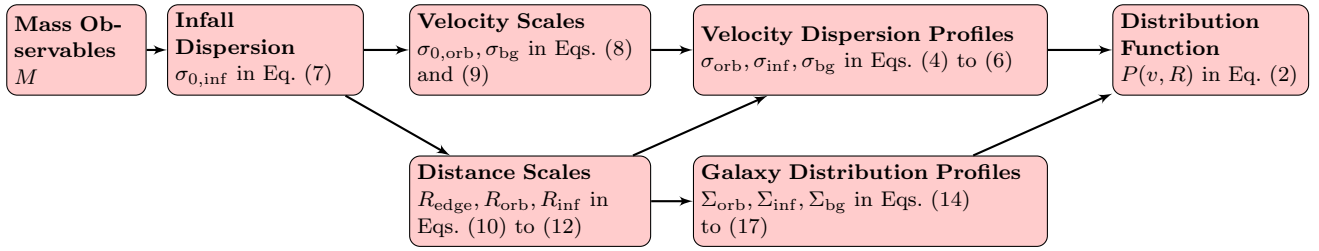


Figure 4. The schematic diagram shows how the velocity distribution function is constructed along with the equations where these quantities are defined. The projected radii and velocities of the galaxies are normalized with cluster mass dependent distance and velocity scales. We then construct the normalized radial profiles of surface densities and velocity dispersions, which define the amplitude and width of the velocity distributions respectively. Table 1 describes the parameters fitted for the model along with the associated physical quantities.

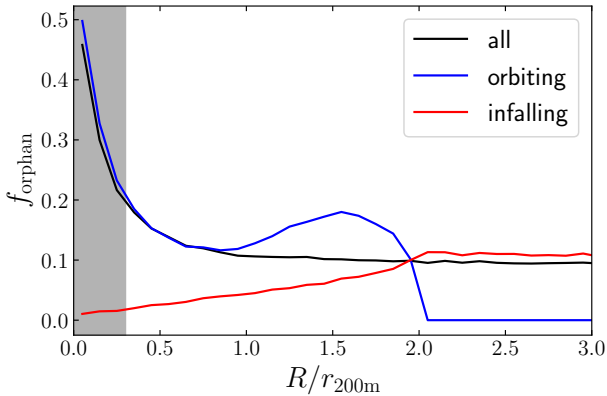


Figure 5. Fraction of the number of orphan galaxies to the total number of galaxies within each sample, all (black), orbiting (blue), or infalling (red) galaxies, as a function of the 2D projected radius. Most of the orphan galaxies are orbiting galaxies residing within $r < 0.3r_{200m}$ (indicated with the grey shaded region). The orphan fraction of orbiting galaxies rises around $1.0 < r/r_{200m} < 1.5$, as the total number of orbiting galaxies decrease drastically. The infalling population, on the other hand, increases monotonically with radius and asymptotes to a constant value of 0.12 at $r/r_{200m} > 2.0$.

3. The figure is restricted to 4 representative radial bins, though we emphasize we fit for the velocity distribution at all radii $R < 3r_{200m}$ simultaneously. The model parameters that we varied for this chain are listed in Table 1, and include all the parameters introduced in our model. We see that our parametric model provides an excellent fit to the data across all cluster radii. We emphasize that the velocity distributions inferred from our model rely exclusively on observables, and do not benefit from an a priori split of galaxies into orbiting and infalling. Note too the lack of an orbiting galaxy population at radii larger than the halo edge radius.

The lines in Fig. 7 show our best fit model for the LOS velocity dispersion of orbiting and infalling galaxies as a function of the projected radius. The data points are the dispersions estimated using orbiting and infalling galaxies only, as tagged based on their orbital properties. The number of degrees of freedom is hard to estimate, since the fit is done at the likelihood level using individual galaxies. We set the degrees of freedom to the number of points (17 and 27 for orbiting and infalling, respectively) minus the number of parameters describing the velocity profile (5 parameters each for the orbiting (σ_{orb}, R_{orb}) and

the infalling (σ_{inf}, R_{inf}) populations in Table 1). The corresponding χ^2/dof are 10.4/12 and 17.3/22 for orbiting and infalling galaxies, respectively. That is, our parametric model provides a statistically acceptable description of the data.

We further demonstrate that our analysis recovers the correct scaling between the mass and each of the three radial scales, R_{edge}, R_{inf} , and R_{orb} and velocity dispersion scales σ_{orb} and σ_{inf} . To do so, we repeat our analysis using only halo–galaxy pairs for halos in narrow mass bins. For this analysis, we modify our model so that $R_{edge}, R_{inf}, R_{orb}, \sigma_{orb}$ and σ_{inf} are constants within each individual mass bin. Fig. 8 shows the recovered values of σ_{inf} and σ_{orb} in each mass bin, along with the best-fit relation from our global model. The errors are determined from the posterior distribution of the fit in each mass bin. The resulting data points are well fit using the proposed power-law model.

Fig. 9 shows the recovered values of $R_{edge}, R_{inf}, R_{orb}$ instead. We see again that the resulting data points are well fit using the proposed power-law model. The calibrated amplitude and slopes of the three relations given the pivot point $1.24 \times 10^{14} M_{\odot}/h$ are

$$\log_{10} R_{p,edge} = 0.505 \pm 0.006, \quad \alpha_{edge} = 1.32 \pm 0.07, \quad (21)$$

$$\log_{10} R_{p,orb} = -0.113 \pm 0.009, \quad \alpha_{orb} = 1.89 \pm 0.05, \quad (22)$$

$$\log_{10} R_{p,inf} = 0.0111 \pm 0.006, \quad \alpha_{inf} = 1.60 \pm 0.08, \quad (23)$$

where the radii are in units of Mpc.

Finally, we turn to examine how the fraction of orbiting and infalling galaxies changes as a function of the halo-centric projected radius R . Fig. 10 compares the fractions inferred from our model to those obtained using the orbiting/infalling split described in §3. As expected, the fraction of orbiting galaxies decreases monotonically with radius, and approaches 0 at R_{edge} . The infall fraction, on the other hand, increases with radius up to $R \lesssim 1.2r_{200m}$ (due to the decreasing number of orbiting galaxies), but then decreases as we move further from the halo as expected. Once again, our best fit model provides an excellent match to the data, with a χ^2/dof of 11.23/14 and 16.48/23 for the orbiting and infalling profiles. As before, the number of degrees of freedom is set to the number of data points (17 for orbiting and 27 for infall and background) minus the number of parameters describing each of surface densities (Σ, R_{edge} in Table 1).

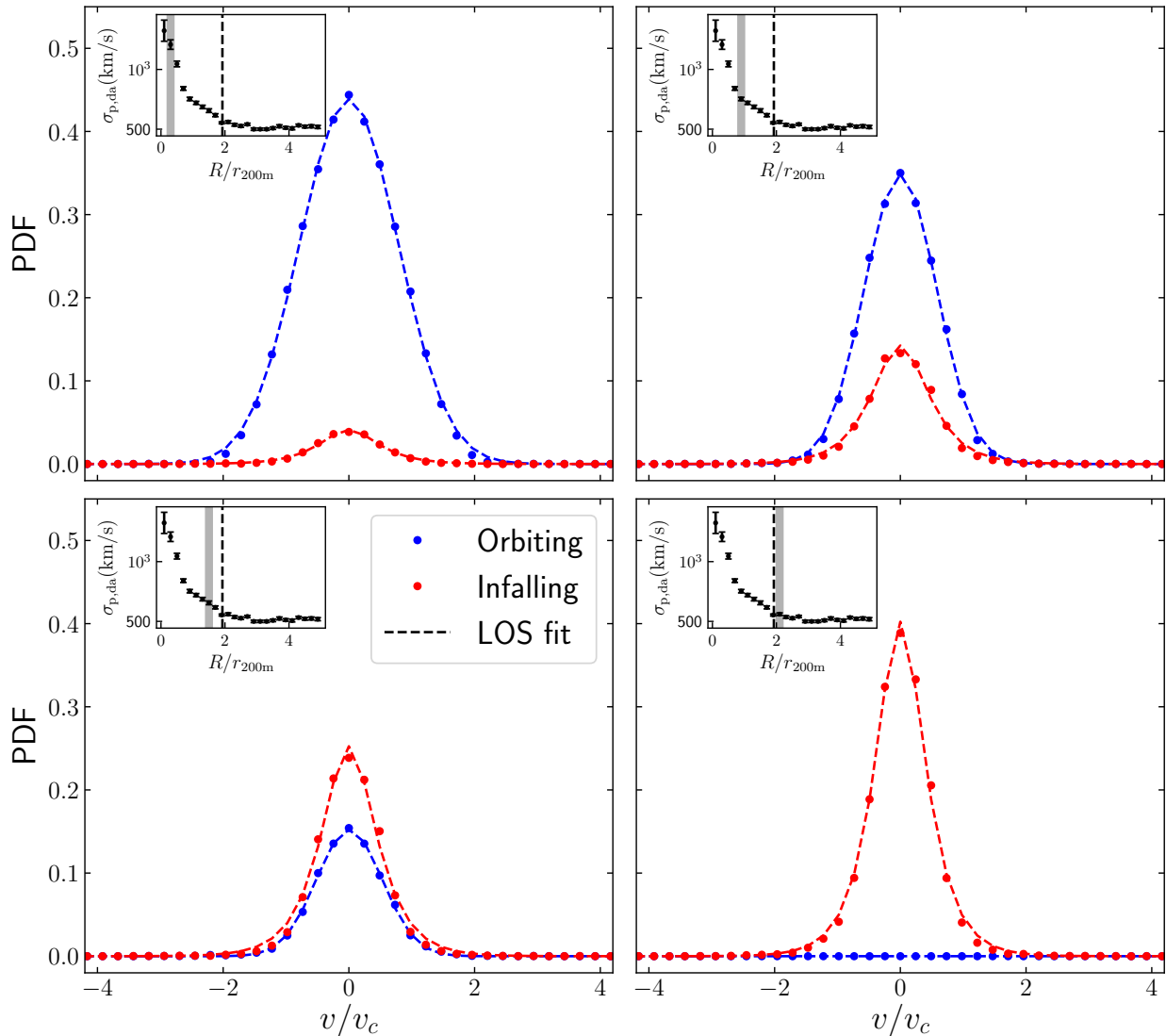


Figure 6. The velocity distributions of the orbiting and infalling components using all galaxies along the line-of-sight (LOS) for four 2D radial shells of $0.2 < R/r_{200m} < 0.4$ (top left panel), $1.1 < R/r_{200m} < 1.3$ (top right panel), $1.6 < R/r_{200m} < 1.8$ (bottom left panel) and $2.0 < R/r_{200m} < 2.2$ (bottom right panel). Note that the first 3 panels correspond to LOS 1 and the bottom right panel to LOS 2 in the schematic diagram in Fig. 1. The horizontal axis is scaled by $v_c = \sqrt{GM_{200m}/r_{200m}}$. The counts are normalized for the total population in each radial bin separately. The lines indicate the distributions obtained by using the fitting procedure described in §4, which relies exclusively on projected data, while the dots are the distributions of orbiting and infalling galaxies based on the pericentric passage, which themselves require the full dynamical history of every galaxy in the sample. The insets show the velocity dispersion profile of orbiting and infalling galaxies combined, along with a shaded band indicating the radial bin of the galaxies shown in the panel. Our model allows us to statistically recover the distribution of orbiting and infalling galaxies from the projected dynamical data alone.

6 IMPLICATIONS FOR HUBBLE CONSTANT MEASUREMENTS WITH GALAXY CLUSTERS

In this work, we identify three dynamically different populations of galaxies, along with three length scales that can be used to infer cluster distances: R_{edge} , R_{orb} , and R_{inf} . Our measurements rely on the fact that each of these three radial scales is tightly correlated with the observed velocity dispersions. In our model, we have chosen to use σ_{inf} as our “base” variable upon which other variables depend, but we could have also picked σ_{orb} . The model described above has the potential to self-calibrate systematic uncertainties in the proposed analysis. For example, baryonic effects and dynamical friction are expected to be small for the dynamics of infalling galaxies which have not yet ex-

perienced environmental effects in the virialized region of clusters. We, therefore, expect σ_{inf} to be much less susceptible to the non-linear cluster astrophysics than σ_{orb} . Thus, the comparison of the edge radius and the other radii scales obtained using multiple observables, such as σ_{inf} and σ_{orb} , may enable us to self-calibrate systematic uncertainties associated with baryonic physics in our proposed measurement. We briefly describe below a possible application of our modeling framework, which we intend to pursue in future work.

Wagoner et al. (2021) argue that: 1) the feature in the velocity dispersion profile of galaxy clusters corresponds to the halo edge radius of the clusters; and 2) that this feature can be used as a standard ruler. Specifically, the predicted error in dimensionless Hubble constant $h = H_0/100\text{km s}^{-1}$

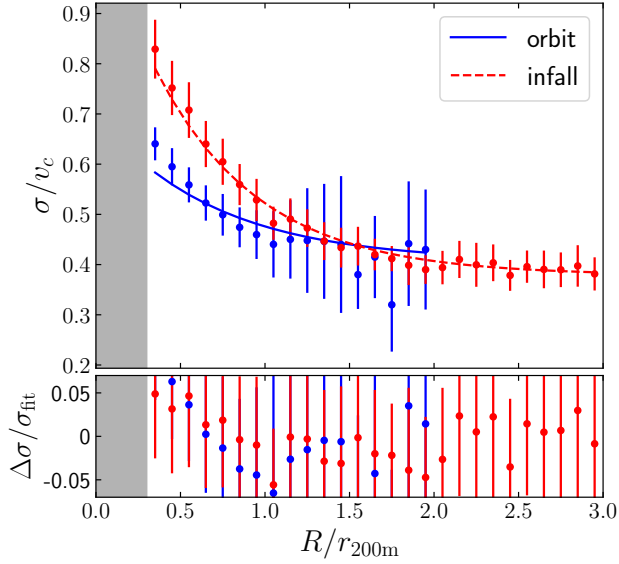


Figure 7. The stacked LOS dispersion profile of orbiting (blue) and infalling (red) galaxies as a function of 2D projected radius for dark matter halos. The data points are measured from the stacked profile, while the errorbars are obtained with jackknife resampling. The bottom panel shows that the best-fit model recovers the velocity dispersion profiles of the orbiting populations. The shaded region has a large fraction of orphan galaxies, and is not included in our fits.

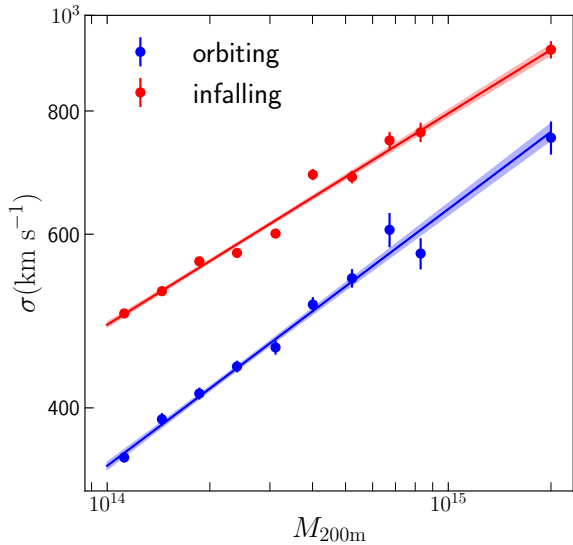


Figure 8. The line-of-sight velocity dispersion-mass relation of the orbiting and infalling galaxies. The data points in the figure represent the values fitted from the stacked profile in logarithmically spaced mass bins. The errorbars represent the error on the fitted values. The line indicates the median best-fit relation. The shaded region indicates (16 – 84)-percentile around the best-fit relation.

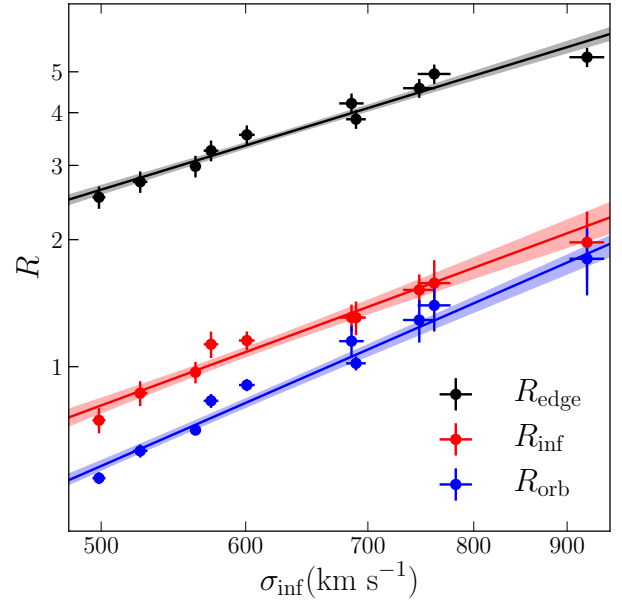


Figure 9. The scaling relations of the radial scales (R_{edge} , R_{orb} , R_{inf}) in units of Mpc as a function of the LOS velocity dispersion of infalling galaxies. The data points in the figure represent the values fitted from the stacked profile in logarithmically spaced mass bins. The errorbars represent the error on the fitted values. The line indicates the median best-fit relation. The shaded region indicates (16 – 84)-percentile around the best-fit relation.

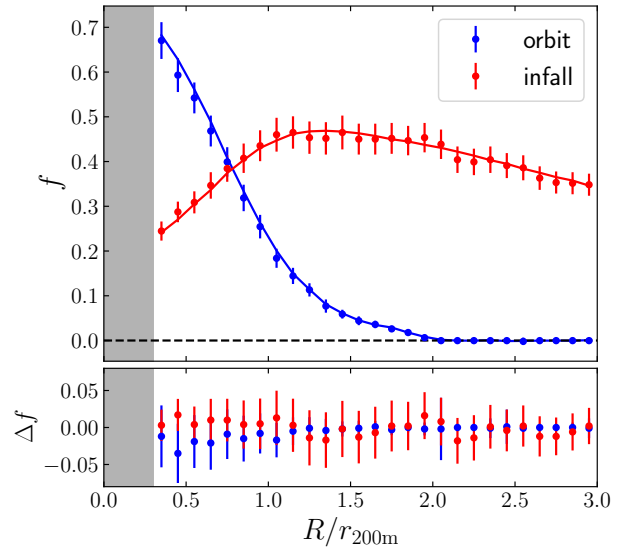


Figure 10. The fraction of the orbiting, and infalling galaxies as a function of projected radius. The data points indicate the measurements from the simulations and the errorbars are obtained with jackknife resampling. The lines indicate the best-fit model for each population. Our fits do not include the shaded region due to the large fraction of orphan galaxies in the cores of halos. These fractions along with the interloper fraction add up to 1, where the interloper fraction increases as a function of the projected radius.

is

$$\sigma_h = \sqrt{\left(\frac{h_{\text{fid}}\sigma_{R_{\text{p,edge}}}}{R_{\text{p,edge}}}\right)^2 + \sigma_{h,\text{fid}}^2}, \quad (24)$$

where $\sigma_{R_{\text{p,edge}}}$ is the error on the simulation calibrated pivot edge radius and $\sigma_{h,\text{fid}}$ is the statistical uncertainty in the recovered cluster edge radius. The latter depends on the specific survey assumptions adopted in the forecast, and was estimated by Wagoner et al. (2021) to be ≈ 0.009 in DESI. To determine the validity of the proposal by Wagoner et al. (2021), we first check whether the edge radius recovered in the projected phase space from our model R_{edge} coincides with the 3D edge radius r_{edge} . The 2D edge radius comes from our likelihood analysis using narrow mass bins. The error in R_{edge} is obtained from the posterior of the fit. The 3D edge radius is the smallest radius containing all orbiting galaxies. Its error is obtained by jackknifing the simulation box. Fig. 11 compares the recovered edge radius R_{edge} to the true, three-dimensional radius r_{edge} determined using the orbiting/infall/background split described in §3. Evidently, our model allows us to correctly recover the three-dimensional edge radius r_{edge} , validating the Wagoner et al. (2021) proposal. Given the calibrated value of $\sigma_{R_{\text{p,edge}}}/R_{\text{p,edge}} = 0.0138$ and $h_{\text{fid}} = 0.67$, the calibration floor on the Hubble parameter when using our simulations is $\sigma_h = 0.0129$.

In addition to edge radius, our method provides three distinct distance scales that can be used to constrain the Hubble parameter. Thus, if we also fix these additional distance scales, we can obtain a tighter constraint. To test this, we generate a mock galaxy catalog where the projected radii are converted to angular distances assuming $h_{\text{fid}} = 0.67$. We then fix the scaling relations of all three radial scales $R_{\text{edge}}, R_{\text{inf}}$, and R_{orb} and fit for the Hubble parameter. We find that the error on the Hubble parameter is reduced by a factor of 2 when using all 3 distance scales, relative to the constraints derived using only R_{edge} .

Naively, the calibration floor in our analysis is larger than the statistical uncertainty of DESI. However, Wagoner et al. (2021) assume that the scaling relations between each of our three radii $R_{\text{edge}}, R_{\text{orb}}$, and R_{inf} , and the velocity dispersions σ_{orb} and σ_{inf} , are cosmology independent. However, if the relations between R – σ depend on the Hubble parameter h , the previously estimated error can either increase or decrease. From the virial theorem, we naively expect $\sigma^2 \propto M/R$. Traditional spherical-overdensity halo definitions take the form of $M \propto \Delta \rho_c R^3$ where ρ_c is the critical density of the Universe and Δ is the average overdensity enclosed within the sphere with a radius R . Since $\rho_c \propto h^2$, we can combine the two equations to arrive at $R \propto h^{-1}\sigma$. If this were the case, then the combination $R(\sigma)/D_A$ would in fact be independent of h , effectively ruining the entire argument. However, it is important to emphasize that: 1) our base velocity dispersion is that of *infalling* galaxies, so the use of the virial theorem is questionable, and 2) the above prediction relies on traditional spherical overdensity halo definitions. These definitions are unphysical, and fail to capture the dynamics of orbiting structures in a halo. Indeed, notice that the above argument also implies that the slope of the R – σ relation is one and that of R – M is one-third. By contrast, the mass-radius relations of the splashback and other similar radius definitions defining the outer boundary do not follow $M \propto R^3$ (More et al. 2015; Garcia et al. 2020), as the overdensity of the splashback Δ introduces additional mass dependence (Diemer et al. 2017; Shi 2016).

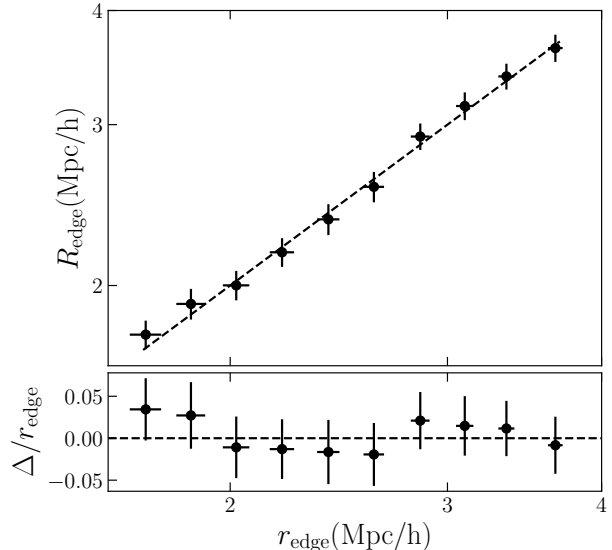


Figure 11. The relation between the three-dimensional edge radius inferred from particle orbits (r_{edge}) and the projected edge radius as inferred from the line-of-sight velocity data (R_{edge}). The data points in the figure represent the values from logarithmically spaced mass bins in the range $10^{14} < M_{200\text{m}}/(M_{\odot}/h) < 10^{15}$. The errorbars on 3D edge radius represent the jackknife error, while the errorbars in the inferred radii are obtained from the posterior. The dashed line indicates the 1-to-1 relation.

Equations 10 through 12 have slopes in the range 1.3 to 1.9, hinting that the dependence on h may not be that of our naive prediction. For our analysis, we will assume that $R_x \propto h^{-1 \pm \alpha_h} \sigma_{0,\text{inf}}^{\alpha_x}$, where α_h indicates deviation from the virial theorem. Then Eq. (24) can be rewritten as

$$\sigma_h = \sqrt{\left(\frac{h_{\text{fid}}\sigma_{R_{\text{p,edge}}}}{R_{\text{p,edge}}}\right)^2 + \left(\frac{\sigma_{h,\text{fid}}}{\alpha_h}\right)^2}. \quad (25)$$

Given the same calibrated value of $\sigma_{R_{\text{p,edge}}}/R_{\text{p,edge}} = 0.0138$, $h_{\text{fid}} = 0.67$, and $\sigma_{h,\text{fid}} = 0.009$, for $\alpha_h = 1$, we recover the original uncertainty with $\sigma_h = 0.0129$. To determine α_h , we employ the Quijote simulations (Villaescusa-Navarro et al. 2020) with $h = 0.6511, 0.6711, 0.6911$. We then select halos with mass above $10^{14} M_{\odot}/h$ as clusters, and randomly subsample the dark matter particles by a factor of 10 to generate a mock sample of “galaxies.” We find R_{edge} in each of the three simulations, and fit our results to a power-law in h . We find that $\alpha_h = 0.78 \pm 0.10$, with a 2.5% error on the Hubble parameter. Taking into account the fact that including additional distance scales will reduce the error by a factor of 2, we expect an error of $\approx 1.3\%$ on the Hubble parameter with the data from the DESI survey.

7 CONCLUSIONS

We present a new parametric model of the projected velocity field of massive dark matter halos, and test it on a mock galaxy catalog produced with UniverseMachine run on the MDPL2 N-body simulation. Our model splits galaxies into three kinematically distinct populations: orbiting, infalling, and background. Each population has a different radially-dependent velocity distribution and surface density profile. Our main findings are as follows:

(i) Our model accurately describes the radially dependent line-of-sight velocity distribution of dark matter halos. In particular, using only projected observables, a likelihood analysis based on our model correctly recovers the velocity distribution of each of the three types of galaxies: orbiting, infalling, and background (see Fig. 6).

(ii) In addition to using R_{edge} , the smallest radius containing all orbiting galaxies, the halo velocity dispersion profile contains two additional length scales R_{orb} and R_{inf} . These two radii govern the drop-off of the orbiting and infalling velocity dispersions as a function of radius (see Fig. 7), and represent two additional cluster scales that can be empirically recovered from the projected velocity dispersion of galaxy clusters.

(iii) The amplitudes of the velocity dispersion profiles σ_{orb} and σ_{inf} are correlated with the cluster scales R_{orb} , R_{inf} , and R_{edge} (see Fig. 9). Calibration of these scaling relations enables us to use these scales as standard rulers, thereby enabling us to measure the Hubble parameter h from projected cluster observables.

(iv) Our model allows us to recover unbiased estimates of the fraction and dispersion of orbiting/infalling galaxies as a function of radius (see Fig. 10). This is, to our knowledge, the first method capable of statistically distinguishing between these two galaxy populations using observable data.

Our work provides the first step toward modeling the projected phase space structure beyond the virial and splashback radius, while taking into account projection effects. We caution that many additional sources of systematic uncertainty remain to be characterized (e.g., miscentering, selection functions, and baryonic effects).

We intend to address each of these in turn in future works, with the goal of realizing a percent-level measurement of the projected velocity distribution using upcoming spectroscopic surveys, such as DESI, PFS, and SPHEREx.

ACKNOWLEDGEMENT

We thank the anonymous referee for helpful comments on the draft. The CosmoSim database used in this paper is a service by the Leibniz-Institute for Astrophysics Potsdam (AIP). The MultiDark database was developed in cooperation with the Spanish MultiDark Consolider Project CSD2009-00064. HA and DN acknowledge support from Yale University and the facilities and staff of the Yale Center for Research Computing. DN and ER also acknowledge funding from the Cottrell Scholar program of the Research Corporation for Science Advancement. ER and BW are supported by DOE grants DE-SC0015975 and DE-SC0009913. ER is also supported by NSF grant 2009401.

DATA AVAILABILITY

The MDPL2 halo catalogs and the mock UM galaxy catalogs are publicly available at <https://www.peterbehroozi.com/data.html>.

REFERENCES

Adhikari S., Dalal N., Chamberlain R. T., 2014, *J. Cosmology Astropart. Phys.*, 11, 19

Allen S. W., Evrard A. E., Mantz A. B., 2011, *ARA&A*, 49, 409

Anbajagane D., et al., 2022, *MNRAS*, 510, 2980

Aung H., Nagai D., Rozo E., García R., 2021, *MNRAS*, 502, 1041

Bakels L., Ludlow A. D., Power C., 2021, *MNRAS*, 501, 5948

Behroozi P. S., Wechsler R. H., Wu H.-Y., 2013a, *ApJ*, 762, 109

Behroozi P. S., Wechsler R. H., Wu H.-Y., Busha M. T., Klypin A. A., Primack J. R., 2013b, *ApJ*, 763, 18

Behroozi P., Wechsler R. H., Hearin A. P., Conroy C., 2019, *MNRAS*, 488, 3143

Bocquet S., et al., 2015, *ApJ*, 799, 214

DESI Collaboration et al., 2016, preprint, ([arXiv:1611.00036](https://arxiv.org/abs/1611.00036))

Diemer B., Kravtsov A. V., 2014, *ApJ*, 789, 1

Diemer B., Mansfield P., Kravtsov A. V., More S., 2017, *ApJ*, 843, 140

Duffy A. R., Schaye J., Kay S. T., Dalla Vecchia C., 2008, *MNRAS*, 390, L64

Evrard A. E., et al., 2008, *ApJ*, 672, 122

Farahi A., Evrard A. E., Rozo E., Rykoff E. S., Wechsler R. H., 2016, *MNRAS*, 460, 3900

Foreman-Mackey D., Hogg D. W., Lang D., Goodman J., 2013, *PASP*, 125, 306

García R., Rozo E., Becker M. R., More S., 2020, arXiv e-prints, p. [arXiv:2006.12751](https://arxiv.org/abs/2006.12751)

Hamabata A., Oguri M., Nishimichi T., 2019, *MNRAS*, 489, 1344

Jiang F., van den Bosch F. C., 2014, preprint, ([arXiv:1403.6827](https://arxiv.org/abs/1403.6827))

Klypin A., Yepes G., Gottlöber S., Prada F., Heß S., 2016, *MNRAS*, 457, 4340

Lam T. Y., Nishimichi T., Schmidt F., Takada M., 2012, *Phys. Rev. Lett.*, 109, 051301

Lam T. Y., Schmidt F., Nishimichi T., Takada M., 2013, *Physical Review D*, 88, 023012

Lau E. T., Nagai D., Kravtsov A. V., 2010, *ApJ*, 708, 1419

More S., Diemer B., Kravtsov A. V., 2015, *ApJ*, 810, 36

Munari E., Biviano A., Borgani S., Murante G., Fabjan D., 2013, *MNRAS*, 430, 2638

Pratt G. W., Arnaud M., Biviano A., Eckert D., Ettori S., Nagai D., Okabe N., Reiprich T. H., 2019, *Space Sci. Rev.*, 215, 25

Shi X., 2016, *MNRAS*, 459, 3711

Springel V., 2005, *MNRAS*, 364, 1105

Tomooka P., Rozo E., Wagoner E. L., Aung H., Nagai D., Sa-fonova S., 2020, *MNRAS*, 499, 1291

Villaescusa-Navarro F., et al., 2020, *ApJS*, 250, 2

Wagoner E. L., Rozo E., Aung H., Nagai D., 2021, *MNRAS*, Walker S., et al., 2019, *Space Sci. Rev.*, 215, 7

Wu H.-Y., Hahn O., Evrard A. E., Wechsler R. H., Dolag K., 2013, *MNRAS*, 436, 460

Zu Y., Weinberg D. H., 2013, *MNRAS*, 431, 3319

Zu Y., Weinberg D. H., Jennings E., Li B., Wyman M., 2014, *MNRAS*, 445, 1885